Available online at www.sciencedirect.com
SCIENCE DIRECT®
Cement & Concrete Composites 27 (2005) 481–492
Cement & Concrete Composites
www.elsevier.com/locate/cemconcomp

Numerical analysis of oblique impact on reinforced concrete

T.L. Teng [a,*], Y.A. Chu [b], F.A. Chang [c], H.S. Chin [d]

[a] Department of Mechanical and Automation Engineering, Da-Yeh University, 112, Shan-Jiau Rd., Da-Tsuen, Changhua 515, Taiwan, ROC
[b] Chung-Shan Institute of Science and Technology, P.O. Box 90008-17-10, Lung-Tan, Tao-Yuan 325, Taiwan, ROC
[c] Department of Civil Engineering, Chung Cheng Institute of Technology, University of National Defense, Ta-Shi, Tao-Yuan 335, Taiwan, ROC
[d] Institute of System Engineering, Chung Cheng Institute of Technology, University of National Defense, Ta-Shi, Tao-Yuan 335, Taiwan, ROC

Received 3 December 2002; accepted 14 May 2004

Abstract

This study proposes a simple but efficient methodology based on the equivalent inclusion method and finite element analysis. Oblique impacting is considered to investigate the residual velocity and ricochet limit of an ogive-nose steel projectile with various impact velocities against a reinforced concrete slab. The computational results are compatible with Tate's formula for the ricochet limit as a function of the impact velocity. The proposed methodology is useful for designing defense structures, and the ricochet limit is one of the important parameters that govern the performance of a weapon system. The methodology can be further developing for designing the protection of military structures and nuclear power plants against high velocity projectiles.

Keywords: Reinforced concrete; Oblique impact; Ricochet limit

1. Introduction

The penetration and perforation of concrete has long been of interest to the military. Recently, it has attracted attention in relation to various other applications, including the design of impact resistant structures for nuclear power plants, various industrial buildings, military bunkers and public facilities, among others. A review of previous work reveals many studies of concrete penetration from the early 1940s. However, most of this work ceased shortly after World War II and was not resumed until the 1960s. Therefore, the penetrability of concrete by projectiles and the resistance of concrete against explosion are of great interest to not only the designers of protective structures but also the developers of weapon systems.

Studies of the penetration and perforation of plain and reinforced concrete are categorized into experimental, empirical or semi-empirical, analytical and numerical simulations. Kasai et al. [1], Hanchak et al. [2], Dancygier and Yankelevsky [3,4] and Gomez and Shuka [5] experimentally investigated the penetration of reinforced concrete targets by steel projectiles with velocities between 150 and 1000 m/s. For plain concrete, various empirical or semi-empirical formulae are available to specify the local effects of perforation, penetration, front face spalling and back face scabbing due to the impact of a projectile [6,7]. The Ballistic Research Laboratory (BRL), the Waterways Experiment Station (WES), the National Defense Research Committee (NDRC), and other organizations have also developed many empirical formulae from experimental data of the penetration of concrete [8]. McMahon et al. [9], Chang [10], Williams [11] and Yankelevsky [12] provided analytical solutions for the critical thickness of concrete panels for with respect to scabbing or perforation. Forrestal and Tzou [13] developed a spherical

* Corresponding author. Tel.: +886 4 8511221; fax: +886 4 8511224.
E-mail addresses: tlteng@mail.dyu.edu.tw, g930406@ccit.edu.tw (T.L. Teng).

0958-9465/$ - see front matter © 2004 Elsevier Ltd. All rights reserved.
doi:10.1016/j.cemconcomp.2004.05.005

cavity-expansion penetration model of a concrete target to predict the depth of penetration of an ogive-nose steel projectile. Sawamoto et al. [14] used the discrete element method to assess the local damage to reinforced concrete structures impacted by rigid and deformable missiles at a velocity of 215 m/s. The complex properties of concrete (which has randomly distributed cracks), makes difficult the development of a relatively accurate material model to predict numerically the penetration and perforation of a concrete target impacted by a projectile. Accordingly, Chu and Wang [15] used the finite element code LS-DYNA2D to calculate the spall damage of a soil backed concrete layer target due to projectile penetration and underground detonation. Chen [16] presented a continuum damage model for the finite element analysis of the penetration of a concrete target, to predict the residual velocity of a steel projectile with an ogive-nose. Ågårdh and Laine [17] used LS-DYNA3D finite element codes to elucidate the performance of fiber concrete against projectiles with high velocity. Schwer and Day [18] developed and improved numeric computational techniques for modeling and simulating the penetration and perforation of concrete slabs and steel plate targets by obliquely impacting, large, deformable projectiles.

Generally, the impact velocity, mass and nose-shape of a projectile as well as the target material, the impact attack-angle and other factors affect the depth and attitude of a projectile after penetration. However, most of these studies are limited to cases in which the impact is normal to the surface of the target. Although normal incidence of the projectile on the target simplifies the impact dynamics, such ideal conditions are rarely satisfied in planetary explorations; a projectile may hit a planetary surface at an oblique angle. Besides, the modeling and numerical simulation of reinforced concrete under an impact at high velocity are much more complex than those of plain concrete. Therefore, this study proposes a simple but efficient methodology based on the equivalent inclusion method and finite element analysis. The reinforced concrete material is ideally transformed into an equivalent material based on the equivalent inclusion method. The equivalent material is homogeneous but anisotropic (or orthotropic), in general. Therefore the finite element meshes for the equivalent material are as simple as those for a plain concrete material. No additional meshes are required for modeling of the reinforcing steel bars (or the layers of steel). The anisotropic (or orthortropic) material properties of the equivalent material due to the reinforcing steel bars in the original concrete can be easily modeled with properly chosen constitutive model in a general purposed finite element codes. Oblique impacting is considered to investigate the residual velocity and ricochet limit of an ogive-nose steel projectile with various impact velocities against a reinforced concrete slab. The computational results are compatible with Tate's formula [19] for the ricochet limit as a function of the impact velocity. The proposed methodology is useful for designing defense structures, and the ricochet limit is one of the important parameters that govern the performance of a weapon system. The methodology is also applicable to designing the protection of military structures and nuclear power plants against high velocity projectiles.

2. Fundamental theorem

This section introduces the equivalent inclusion method [20,21] and applies it to a structure of reinforced concrete (for example, a shelter) as an an-isotropic homogeneous material. The inhomogeneities (the reinforcing steel bars) are equivalent to inclusions of identical configurations but hypothetic internal eigenstrains. The tensor product of the eigenstrains and the Eshelby's tensors formulates the strain fields in the inclusions. Mori–Tanaka's mean field theory [22] is then applied to account for the overall stress–strain relations and derive the equivalent material compliance matrix as a function of not only the material moduli of concrete and the reinforcing steel bars, but also the volume fractions and the orientations of the inhomogeneities.

The embedded reinforcing steel bars are defined as equivalent inclusions with hypothetic eigenstrains to construct an equivalent inclusion model of reinforced concrete structures. The shapes of the steel bars are also simplified to cylinders of infinite length, enabling a closed form solution involving Eshelby's tensor to be determined. The basic assumptions of the model are as follows.

1. The interfaces between the matrix and the inclusions are ideally integrated.
2. The matrix and inclusions are elastic, following the generalized Hook's law.
3. All the inclusions have regular shapes and aligned in parallel in one or two orthogonal directions in the matrix.
4. The interactions among inclusions are negligible.

Theoretically, the aggregates, voids, etc., can also be treated as different inhomogeneities embedded in the cement matrix to evaluate the material strength of concrete by the equivalent inclusion method macroscopically [23]. However, in this paper the concrete matrix is considered to be homogeneous isotropic material for the engineering purpose of simplification. Since the material moduli of plain concrete, e.g., the Young's modulus and the Poisson's ratio are much easier attainable from tests and design handbooks than that of reinforced concrete.

2.1. Equivalent inclusion method

Consider a finite region of a composite body D that contains an inhomogeneity with elastic moduli of C^*_{ijkl}, as depicted in Fig. 1. The domain of the inhomogeneity is denoted as Ω. The matrix is denoted by $D-\Omega$ with elastic moduli of C_{ijkl}. Assume the finite region of composite body D is subjected to a uniform surface traction $t^\infty_j = \sigma^\infty_{ij} n_i$ where σ^∞_{ij} is the associated stress field and n_i is the outward unit normal on the boundary of D. If the inhomogeneity is not present in the domain D, then the uniform strains in D are ε^∞_{mn} and the corresponding uniform stresses are $\sigma^\infty_{ij} = C_{ijkl}\varepsilon^\infty_{kl}$. When the inhomogeneity Ω is present in D, the stress disturbances in the matrix and inclusion are represented by σ^M_{ij} and σ^Ω_{ij}, respectively. The corresponding strain disturbances are denoted as ε^M_{mn} and ε^Ω_{ij}, respectively. Hook's law is written as,

$$\sigma^\infty_{ij} + \sigma^\Omega_{ij} = C^*_{ijmn}\{\varepsilon^\infty_{mn} + \varepsilon^\Omega_{mn}\} \quad \text{in } \Omega \tag{1a}$$

$$\sigma^\infty_{ij} + \sigma^M_{ij} = C_{ijmn}\{\varepsilon^\infty_{mn} + \varepsilon^M_{mn}\} \quad \text{in } D-\Omega \tag{1b}$$

Let the inhomogeneity be replaced by an inclusion with the same elastic moduli C_{ijkl} as the matrix and with an equivalent eigenstrain ε^*_{mn}. Hook's law for the equivalent inclusion is,

$$\sigma^\infty_{ij} + \sigma^\Omega_{ij} = C_{ijmn}\{\varepsilon^\infty_{mn} + \varepsilon^\Omega_{mn} - \varepsilon^*_{mn}\} \quad \text{in } \Omega \tag{2}$$

Based on the equivalent inclusion method, the necessary and sufficient condition for the equivalency of the stresses and strains in the inhomogeneity and the equivalent inclusion is,

$$C^*_{ijmn}\{\varepsilon^\infty_{mn} + \varepsilon^\Omega_{mn}\} = C_{ijmn}\{\varepsilon^\infty_{mn} + \varepsilon^\Omega_{mn} - \varepsilon^*_{mn}\} \quad \text{in } \Omega \tag{3}$$

2.2. Strain field of the equivalent inclusion

Now, consider domain D that contains an ellipsoidal inhomogeneity Ω, defined as,

$$\Omega: \quad \frac{x_1^2}{a_1^2} + \frac{x_2^2}{a_2^2} + \frac{x_3^2}{a_3^2} \leqslant 1 \tag{4}$$

where a_1, a_2, and a_3 are the semi-axes of the ellipsoid depicted in Fig. 2. Based on the equivalent inclusion method, the inhomogeneity is equivalent to an inclusion with uniform eigenstrains ε^*_{ij}. According to the Eshelby's solution [24], the associated strain disturbance due to the presence of the strain ε_{ij} within the inclusion is,

$$\varepsilon_{ij} = S_{ijmn}\varepsilon^*_{mn} \quad \text{in } \Omega \tag{5}$$

where S_{ijmn} is Eshelby's tensor, a function of the material moduli of the surrounding matrix C_{ijkl} and the geometry configuration of the inclusion. In the case of isotropic matrix and inclusion, Eshelby's tensor for an elliptic cylinder with $a_1 \to \infty$ and for a cylinder ($a_2 = a_3$) is written as,

$$\begin{aligned}
S_{1111} &= 0\\
S_{1122} &= 0\\
S_{1133} &= 0\\
S_{2222} &= \frac{1}{2(1-v)}\left\{\frac{a_3^2 + 2a_2a_3}{(a_2+a_3)^2} + (1-2v)\frac{a_3}{a_2+a_3}\right\} = \frac{5-4v}{8(1-v)}\\
S_{3333} &= \frac{1}{2(1-v)}\left\{\frac{a_2^2 + 2a_2a_3}{(a_2+a_3)^2} + (1-2v)\frac{a_2}{a_2+a_3}\right\} = \frac{5-4v}{8(1-v)}\\
S_{2233} &= \frac{1}{2(1-v)}\left\{\frac{a_3^2}{(a_2+a_3)^2} - (1-2v)\frac{a_3}{a_2+a_3}\right\} = \frac{-1+4v}{8(1-v)}\\
S_{3311} &= \frac{1}{2(1-v)}\left(\frac{2va_2}{a_2+a_3}\right) = \frac{v}{2(1-v)}\\
S_{3322} &= \frac{1}{2(1-v)}\left\{\frac{a_2^2}{(a_2+a_3)^2} - (1-2v)\frac{a_2}{a_2+a_3}\right\} = \frac{-1+4v}{8(1-v)}\\
S_{2323} &= \frac{1}{2(1-v)}\left\{\frac{a_2^2 + a_3^2}{2(a_2+a_3)^2} + \frac{1-2v}{2}\right\} = \frac{3-4v}{8(1-v)}\\
S_{3131} &= \frac{a_2}{2(a_2+a_3)} = \frac{1}{4}\\
S_{1212} &= \frac{a_3}{2(a_2+a_3)} = \frac{1}{4}\\
S_{2211} &= \frac{1}{2(1-v)}\left(\frac{2va_3}{a_2+a_3}\right) = \frac{v}{2(1-v)}
\end{aligned} \tag{6}$$

where v is Poisson's ratio of the matrix.

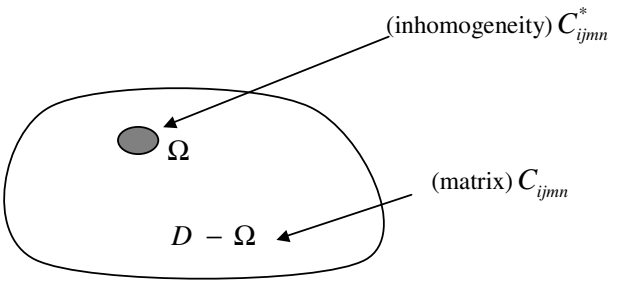

Fig. 1. Matrix and inhomogeneity.

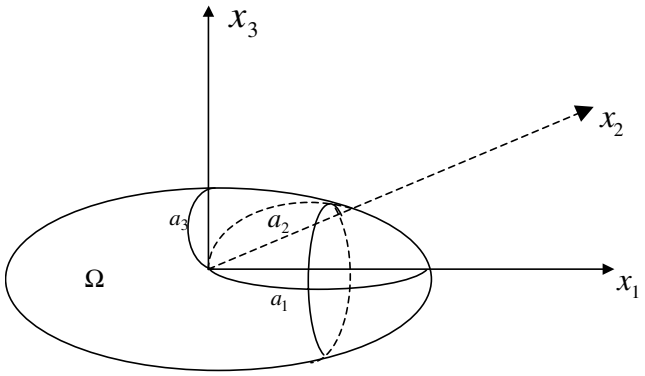

Fig. 2. An ellipsoidal inhomogeneity with principal half axes a_1, a_2 and a_3.

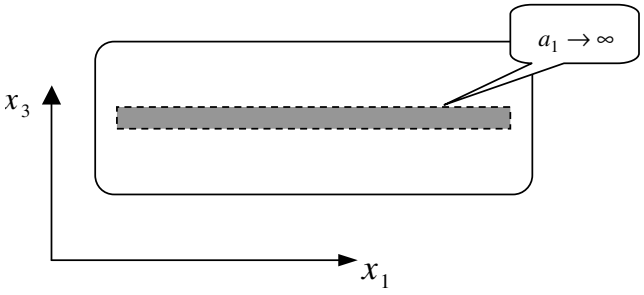

Fig. 3. One-way parallel-aligned cylindrical inhomogeneties ($a_2 = a_3$).

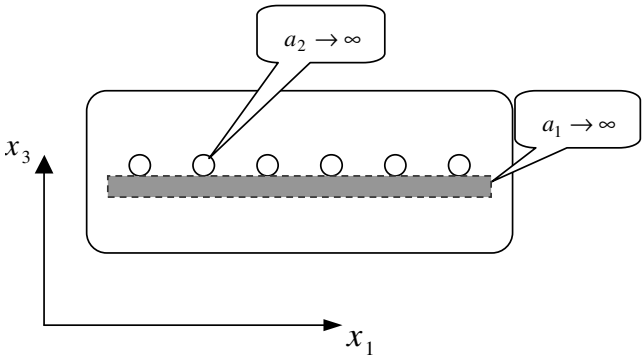

Fig. 4. Two-way orthogonal arrangement of cylindrical inhomogeneities.

If domain D contains N inhomogeneities are of the same shape and the same material properties, then the average values of strains shall be identical over each inhomogeneities [25]. This paper presents two arrangements of the reinforcing steel bars. The first set of one-way parallel-aligned reinforcing steel bars embedded in the concrete (matrix) are modeled as a series of cylindrical inhomogeneities, as in Fig. 3. The second set of two-way orthogonal-aligned steel bars are modeled as in Fig. 4. Eshelby's tensor in the perpendicular direction ($a_2 \to \infty$ and $a_1 = a_3$) can be easily obtained by cyclically permuting the sub-indices $(1,2,3)$ in Eq. (6).

2.3. Equivalent elastic compliance tensor

This section examines the equivalent material compliance tensor for an isotropic elastic matrix with multiphase inclusions, based on Mori–Tanaka's mean field theory [26].

Consider a finite but sufficiently large region of composite body D, containing N distinctly shaped, randomly distributed, ellipsoidal or elliptic cylindrical inhomogeneities $\Omega = \sum_{K=1}^{N} \Omega_K$. The Kth inhomogeneity has elastic moduli C_{ijkl}^{*K} and volume fraction f_K. The surrounding matrix is denoted by $D - \Omega$ and has elastic moduli C_{ijkl}.

Assume that the body is subjected to uniform surface traction $t_j^{\infty} = \sigma_{ij}^{\infty} n_i$. When no inhomogeneities are in the domain, the uniform strain in the composite body is $\underline{\varepsilon}^{\infty}$ and the corresponding uniform stress will be $\underline{\sigma}^{\infty} = \underline{\underline{C}}\,\underline{\varepsilon}^{\infty}$. If the N inhomogeneities are all present in the domain, then the stress disturbances in the matrix and the Kth inclusion are represented as $\underline{\sigma}^{M}$ and $\underline{\sigma}_K^{\Omega}$, respectively. The corresponding average strain disturbances are denoted as $\overline{\underline{\varepsilon}}^{M}$ and $\overline{\underline{\varepsilon}}_K^{\Omega}$. Therefore, the average stress can be written as,

$$\underline{\sigma}^{\infty} + \overline{\underline{\sigma}}^{M} = \underline{\underline{C}}\left[\underline{\varepsilon}^{\infty} + \overline{\underline{\varepsilon}}^{M}\right] \quad \text{in } D - \Omega \tag{7}$$

and the average stress in the Kth inclusion can be written as,

$$\begin{aligned} \underline{\sigma}^{\infty} + \overline{\underline{\sigma}}_K^{\Omega} &= \underline{\underline{C}}_K^{*}\left[\underline{\varepsilon}^{\infty} + \overline{\underline{\varepsilon}}^{M} + \overline{\underline{\varepsilon}}_K\right] \\ &= \underline{\underline{C}}\left[\underline{\varepsilon}^{\infty} + \overline{\underline{\varepsilon}}^{M} + \overline{\underline{\varepsilon}}_K - \underline{\varepsilon}_K^{*}\right] \quad \text{in } \Omega_K \end{aligned} \tag{8}$$

where $\overline{\underline{\varepsilon}}_K = \overline{\underline{\varepsilon}}_K^{\Omega} - \overline{\underline{\varepsilon}}^{M}$ is the average strain disturbance in the Kth inclusion due to the presence of the Kth inhomogeneity itself and $\underline{\varepsilon}_K^{*}$ is the hypothetic equivalent eigenstrain of the Kth inclusion. Note that $\overline{\underline{\varepsilon}}_K^{\Omega}$ is the average strain disturbance of the Kth inclusion, due to the presence of N inhomogeneities. Since the surface traction is uniform and the inclusions are ellipsoidal, the strain disturbances $\overline{\underline{\varepsilon}}_K$ are uniformly distributed, such that $\overline{\underline{\varepsilon}}_K = \underline{\varepsilon}_K$. According to Eshelby's solution, $\underline{\varepsilon}_K = \underline{\underline{S}}_K \underline{\varepsilon}_K^{*}$, where $\underline{\underline{S}}_K$ is Eshelby's tensor for the Kth inclusion due to its own presence of the inclusion.

Based on Mori–Tanaka's mean field theory [22], the volume average of the disturbed stresses must vanish, yielding,

$$\left[1 - \sum_{K=1}^{N} f_K\right] \overline{\underline{\sigma}}^{M} + \sum_{K=1}^{N} f_K \overline{\underline{\sigma}}_K^{\Omega} = 0 \tag{9}$$

Thus, the overall strain field, $\underline{\varepsilon}^{D}$, of the composite body D can be derived as [24],

$$\underline{\varepsilon}^{D} = \underline{\varepsilon}^{\infty} + \sum_{K=1}^{N} f_K \underline{\varepsilon}_K^{*} = \overline{\underline{\underline{C}}}^{-1}\,\underline{\sigma}^{\infty} \tag{10}$$

where $\overline{\underline{\underline{C}}}^{-1}$ is the equivalent elastic compliance tensor and is written as,

$$\overline{\underline{\underline{C}}}^{-1} = \left[\underline{\underline{I}} - \sum_{K=1}^{N} f_K \underline{\underline{P}}_K^{-1}\left(\underline{\underline{C}}_K^{*} - \underline{\underline{C}}\right)\right] \underline{\underline{C}}^{-1} \tag{11}$$

where $\underline{\underline{P}}_K$ is defined as,

$$\underline{\underline{P}}_K = \left(\underline{\underline{C}}_K^{*} - \underline{\underline{C}}\right)\left[\underline{\underline{S}}_K - \sum_{K=1}^{N} f_K\left(\underline{\underline{S}}_K - I\right)\right] + \underline{\underline{C}} \tag{12}$$

and $\underline{\underline{I}}$ is the identity tensor or the so-called unit tensor.

For the case of a single-phase inclusion (i.e., $N = 1$), Eqs. (11) and (12) can be rewritten as,

$$\overline{C}^{-1}_{mnij} = [I_{mnab} - fP^{-1}_{mnqr}(C^{*}_{qrab} - C_{qrab})]C^{-1}_{abij} \tag{13}$$

and,

$$P^{-1}_{ijab} = \{(C^{*}_{ijmn} - C_{ijmn})[(1-f)S_{mnab} + fI_{mnab}] + C_{ijab}\}^{-1} \tag{14}$$

Similarly based on Mori–Tanaka's mean field theory, the volume average of the disturbed strains must vanish, yielding,

$$\underline{\underline{\overline{C}}} = \underline{\underline{C}}\left[\underline{\underline{I}} + \sum_{K=1}^{N} f_K \underline{\underline{T}}^{-1}_{K}(\underline{\underline{C}}^{*}_{K} - \underline{\underline{C}})\right] \tag{15}$$

where $\underline{\underline{\overline{C}}}$ is the equivalent elastic stiffness tensor and $\underline{\underline{T}}_K$ is given by,

$$\underline{\underline{T}}_K = (\underline{\underline{C}}^{*}_{K} - \underline{\underline{C}})\underline{\underline{S}}_K - \sum_{K=1}^{N} f_K(\underline{\underline{C}}^{*}_{K} - \underline{\underline{C}})\underline{\underline{S}}_K + \underline{\underline{C}} \tag{16}$$

2.4. Equivalent compliance tensor of reinforced concrete slabs

Embedded reinforcing steel bars in reinforced concrete slabs are generally in a two-way orthogonal arrangement, as depicted in Fig. 4. Therefore, in this section Eqs. (11) and (12) are applied to demonstrate the calculation of the equivalent elastic compliance tensor for the reinforced concrete slabs. From Eq. (11), the elastic compliance tensor for reinforced concrete with steel bars in a two-phase orthogonal arrangement can be shown as,

$$\underline{\underline{\overline{C}}}^{-1} = \left[\underline{\underline{I}} - f_1\underline{\underline{P}}^{-1}_{1}(\underline{\underline{C}}^{*}_{1} - \underline{\underline{C}}) - f_2\underline{\underline{P}}^{-1}_{2}(\underline{\underline{C}}^{*}_{2} - \underline{\underline{C}})\right]\underline{\underline{C}}^{-1} \tag{17}$$

where

$$\underline{\underline{P}}^{-1}_{1} = \left\{(\underline{\underline{C}}^{*}_{1} - \underline{\underline{C}})\left[\underline{\underline{S}}_1 - f_1(\underline{\underline{S}}_1 - I) - f_2(\underline{\underline{S}}_2 - I) + C\right]\right\}^{-1} \tag{18}$$

$$\underline{\underline{P}}^{-1}_{2} = \left\{(\underline{\underline{C}}^{*}_{2} - \underline{\underline{C}})\left[\underline{\underline{S}}_2 - f_1(\underline{\underline{S}}_1 - I) - f_2(\underline{\underline{S}}_2 - I) + C\right]\right\}^{-1} \tag{19}$$

Sub-indices 1 and 2 represent the two phases of mutually orthogonal cylindrical inhomogeneities with axes in directions of the coordinate axes x_1 and x_2, respectively.

For the two-way orthogonal arrangement of reinforcing steel bars that have the same shape and material properties $\underline{\underline{C}}^{*}_{1} = \underline{\underline{C}}^{*}_{2}$; Eshelby's tensor $\underline{\underline{S}}_2$ can be obtained from $\underline{\underline{S}}_1$ in Eq. (6) by cyclic permutation of the indices $(1,2,3)$. Using Voight notation, the orthotropic equivalent compliance tensor $\underline{\underline{\overline{C}}}^{-1}$ can be further transferred into a 6×6 matrix,

$$[\underline{\underline{\overline{C}}}]^{-1} = \begin{bmatrix} \frac{1}{\overline{E}_{11}} & \frac{-\overline{\nu}_{21}}{\overline{E}_{22}} & \frac{-\overline{\nu}_{31}}{\overline{E}_{33}} & 0 & 0 & 0 \\ \frac{-\overline{\nu}_{12}}{\overline{E}_{11}} & \frac{1}{\overline{E}_{22}} & \frac{-\overline{\nu}_{32}}{\overline{E}_{33}} & 0 & 0 & 0 \\ \frac{-\overline{\nu}_{13}}{\overline{E}_{11}} & \frac{-\overline{\nu}_{23}}{\overline{E}_{22}} & \frac{1}{\overline{E}_{33}} & 0 & 0 & 0 \\ 0 & 0 & 0 & \frac{1}{\overline{G}_{23}} & 0 & 0 \\ 0 & 0 & 0 & 0 & \frac{1}{\overline{G}_{31}} & 0 \\ 0 & 0 & 0 & 0 & 0 & \frac{1}{\overline{G}_{12}} \end{bmatrix} \tag{20}$$

where $\overline{E}_{ij}$, $\overline{G}_{ij}$ and $\overline{\nu}_{ij}$ are the equivalent elastic moduli; the equivalent shear moduli and the equivalent Poisson's ratio of the equivalent reinforced concrete. The value can be determined by comparing Eqs. (17) and (20).

The equivalent material is homogeneous but orthotropic, which can be modeled with properly chosen constitutive model in a general purposed finite element codes. With these transformations based on the equivalent inclusion method, the finite element meshes for the equivalent material of a reinforced concrete slab are as simple as those for a plain concrete material. No additional meshes are required for modeling of the reinforcing steel bars (or the layers of steel).

3. Numerical verification

This section considers the normal impact of an ogive-nose steel projectile at velocities from 300 to 1000 m/s, on a reinforced concrete slab to demonstrate the performance of the proposed model and thus verify the accuracy of the calculation procedure. Fig. 5 depicts a 25.4 mm caliber steel projectile with a total length of 143.7 mm. The steel projectile is assumed to be elastic perfectly plastic with a mass density of 8000 kg/m^3, an elastic modulus of 206.9 GPa, a Poisson's ratio of 0.3 and a yield stress of 1.724 GPa. Fig. 6 presents 610 mm × 610 mm × 178 mm reinforced concrete. The target consists of three orthogonal layers of square grids of reinforcing steel bars with a diameter of 5.69 mm. The original concrete material properties of the target, including density, elastic moduli, and Poisson's ratio are taken to be 2520 kg/m^3, 20.68 GPa and 0.18, respectively. The steel bars used here have density, elastic moduli, and Poisson's ratio of 7850 kg/m^3, 199 GPa and 0.3, respectively.

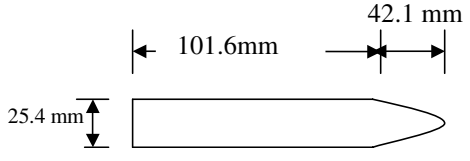

Fig. 5. Steel penetrator geometry.

3.1. Effective material moduli of the target

This subsection determines the equivalent material moduli using the equivalent inclusion method described in Section 2.

First, Eshelby's tensors $\underline{\underline{S}}_1$ and $\underline{\underline{S}}_2$ for the reinforced concrete slab are determined by directly substituting Poisson's ratio of the matrix (the original concrete) into Eq. (6). Table 1 presents the data for $\underline{\underline{S}}_1$ and $\underline{\underline{S}}_2$. Substituting the values of $\underline{\underline{S}}_1$ and $\underline{\underline{S}}_2$ and the associated volume fractions $f_1 = f_2 = 0.005$ into Eqs. (17)–(19) yields the equivalent compliance tensor $\overline{\underline{\underline{C}}}^{-1}$. Finally, the associated equivalent elastic moduli $\overline{E}_{ij}$, shear moduli $\overline{G}_{ij}$ and Poisson's ratio $\overline{\nu}_{ij}$ of the reinforced concrete material are determined from Eq. (20), and listed in Table 2. The equivalent material is orthotropic because the reinforcing steel bars are aligned orthogonally in the concrete slab. Since the volume fractions are equal, $f_1 = f_2$, and the components of the material moduli in directions x_1 and x_2 are equal.

Table 1
Eshelby's tensor

$a_1 \to \infty$ ($a_2 = a_3$)		$a_2 \to \infty$ ($a_1 = a_3$)	
Matrix Poisson's ratio	0.18	Matrix Poisson's ratio	0.18
$S_{1111} = S_{1122} = S_{1133}$	0	$S_{2211} = S_{2222} = S_{2233}$	0
$S_{2211} = S_{3311}$	0.1097	$S_{1122} = S_{3322}$	0.1097
$S_{2233} = S_{3322}$	−0.0426	$S_{1133} = S_{3311}$	−0.0426
$S_{2222} = S_{3333}$	0.6524	$S_{1111} = S_{3333}$	0.6524
S_{2323}	0.3475	S_{3131}	0.3475
$S_{3131} = S_{2121}$	0.25	$S_{2323} = S_{1212}$	0.25

Table 2
Equivalent reinforced concrete material properties

Density	2565 kg/m^3
Sprincipal elastic modulus $\overline{E}_{11}$	20.8 Gpa
Principal elastic modulus $\overline{E}_{22}$	20.8 Gpa
Principal elastic modulus $\overline{E}_{33}$	20.7 Gpa
Poisson's ratio $\overline{\nu}_{12}$	0.175
Poisson's ratio $\overline{\nu}_{13}$	0.175
Poisson's ratio $\overline{\nu}_{23}$	0.172
Shear modulus $\overline{G}_{12}$	9 Gpa

3.2. Finite element model

Fig. 7 depicts the finite element model of the normal impact of an ogive-nose steel projectile, at velocities from 300 to 1000 m/s, on a reinforced concrete slab. For reasons of symmetry, only one-half of the cross-section is modeled using 5177 quadrilateral elements and 5363 nodes, to approximate the target under a plane strain assumption. An erosion algorithm is implemented to solve the excessive element distortion problem and model the fracture of the reinforced concrete target. Two erosion criteria, shear failure and tensile cut-off, are incorporated in the finite element code as follows.

$$\overline{\varepsilon}' = \sqrt{\frac{2}{s} 3\varepsilon'_{ij}\varepsilon'_{ij}} \geqslant f_s \tag{21}$$

$$\varepsilon_{kk} \geqslant f_t \tag{22}$$

where $\varepsilon'_{ij} = \varepsilon_{ij} - \varepsilon_{kk}/3$ are the deviatoric strains; $\overline{\varepsilon}'$ is defined as the effective shear strain; ε_{kk} represents the volumetric strain, and f_s and f_t are the shear erosion strain and the tensile erosion strain, respectively. Coupling Eqs. (21) and (22), the erosion algorithm infinite element code simulates the physical separation of the material. Then one of the two erosion conditions is satisfied; the

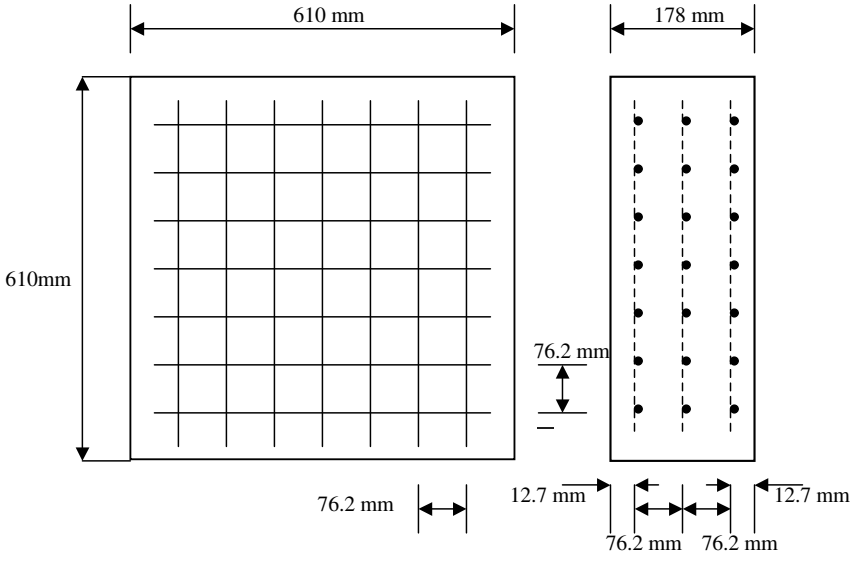

Fig. 6. Reinforced concrete target geometry.

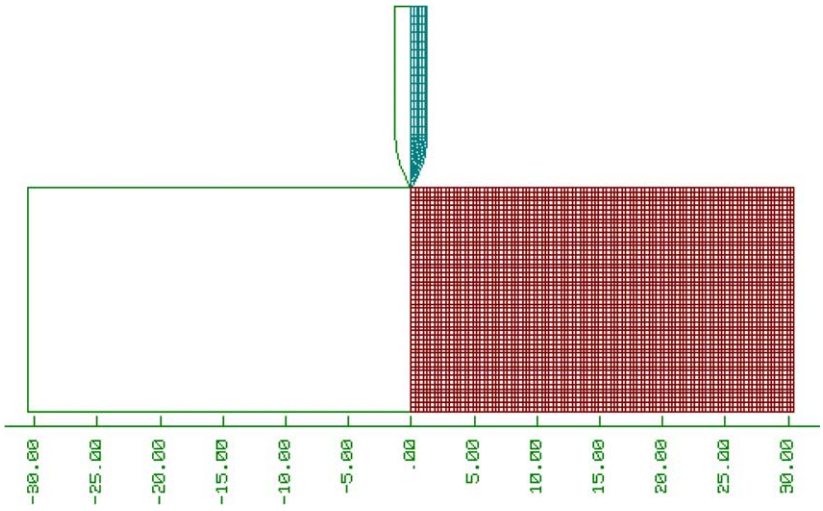

Fig. 7. Finite element model for perforation calculations.

erosion alogrithm removes the associated element. Erosion strains f_s and f_t are both just hypothetical values used in the numerical simulation, but they are not determined using field experimental data. In this example, the erosion strains f_s and f_t are both selected as 0.075. They are first determined by matching the numerically calculated residual velocity to the measured data for a few—normally one or two specific impact velocities. Then, the same criteria are used to calculate numerically other impact velocities.

In this paper, another function of the erosion criteria is to compensate the inability of the equivalent inclusion method for handling the failure behavior of materials. Therefore, the equivalent material is assumed to be linear-elastic upto failure, which is expected to be viable for modeling the tensile and shear fractures of the concrete slab under impact loadings.

3.3. Numerical results of normal impact

The strength of reinforced concrete, a structural material, under compression is higher than that under tension. When a concrete target is overstressed under the impact of projectile, it fails in a brittle, rather than in a ductile manner. When a massive reinforced concrete slab takes a direct hit, the forces generated upon impact and during penetration can easily break up large masses of reinforced concrete, unless sufficient reinforcing steel is available to inhibit the spread of the cracks. Consequently, reinforcement tends to counteract the brittleness of the concrete and confer tensile strength.

Fig. 8(a) and (b) present deformed mesh plots at different stages of the penetration of a steel projectile into a reinforced concrete slab at 382 m/sec. The penetration of the projectile is simulated in two simple stages. In the first stage, (Fig. 8(a)) up to 300 μs, the projectiles partially penetrate the target and only slightly affect the rear face of the slab. When the shock front that travels ahead of the projectile meets the rear boundary, curved shear cracks are developed and a bell-shaped scabbing part is formed.

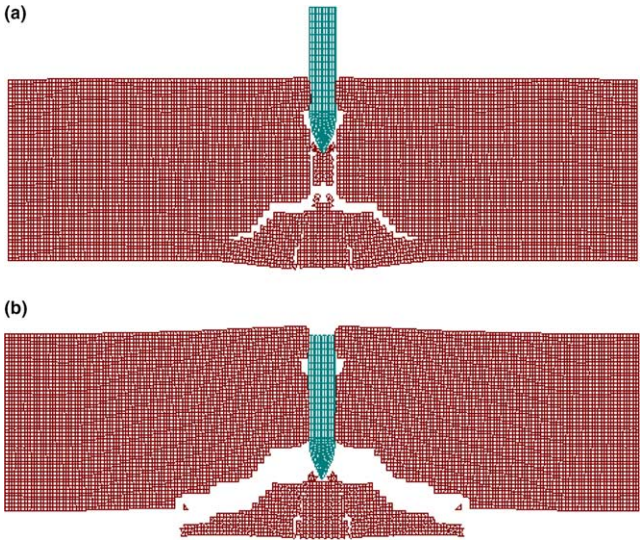

Fig. 8. (a) Normal penetration, stage I ($t = 300\,\mu s$). (b) Normal penetration, stage II ($t = 1050\,\mu s$).

In the second stage, (Fig. 8(b)) up to 1050 μs, the projectile pushes the scabbing part, shears it off the surrounding material and continues to penetrate the slab. The thickness of the perforation is that required to penetrate and completely shear off the scabbing part, and completely stop the projectile and the scabbing part at the end of that process.

When the impact velocity increases to 743 m/s, the reinforced concrete slab is perforated, as shown in Fig. 9 at 320 μs after impact. Cratering and tunneling

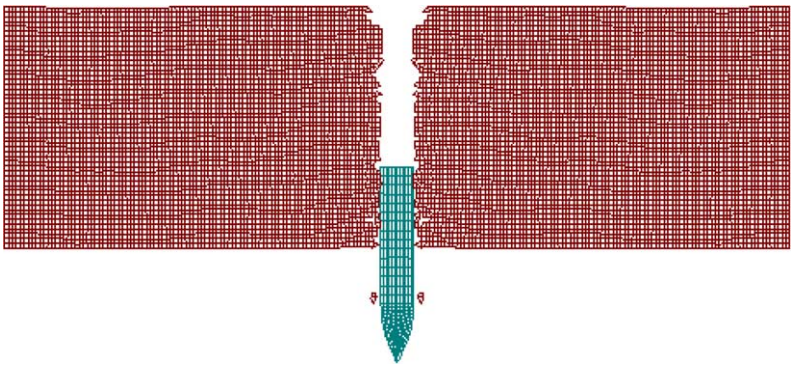

Fig. 9. Deformed mesh plot for 743 m/s impact velocity at 420 μs.

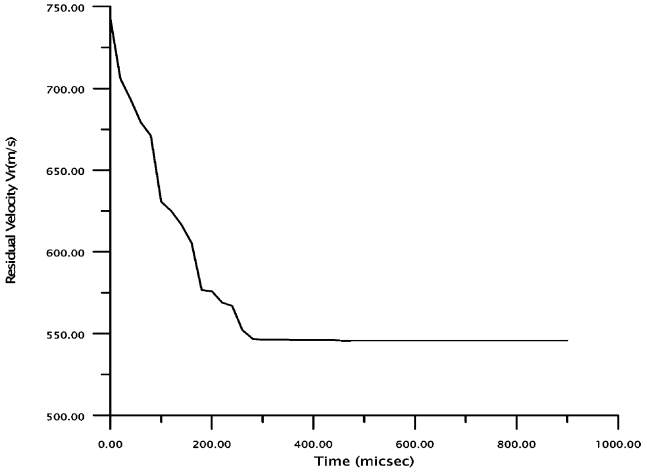

Fig. 10. Penetration velocity history at 743 m/s impact velocity.

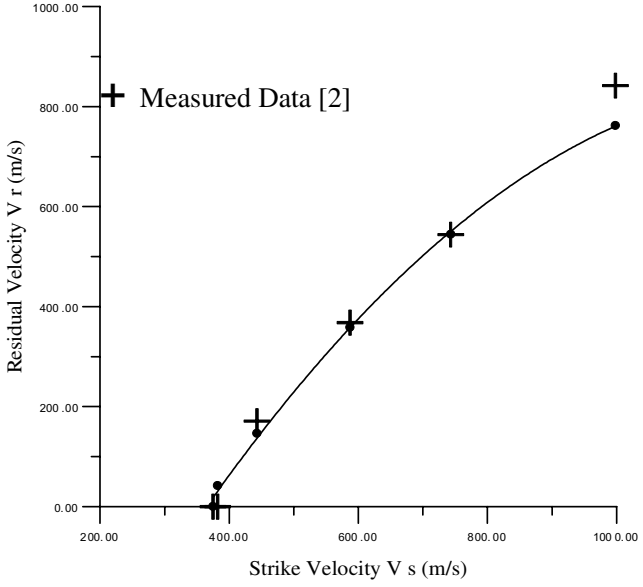

Fig. 11. Comparison of FEA numerical results and test data of Hanchak [2].

phenomena are generated in the slab. Fig. 10 plots a typical history of velocity of the projectile. The velocity of the projectile slowly declines until the slab is perforated. After perforation, the velocity of the projectile remains constant. In this paper, the constant velocity is defined as the residual velocity of the projectile. If the slab is not perforated, then the residual velocity will be zero, implying that the projectile is embedded in the target.

A series of calculations were performed to predict the residual velocities of an ogive-nose steel projectile that impacts a reinforced concrete slab at velocities from 300 to 1000 m/s. Fig. 11 compares the numerical results with the test data of Hanchak et al. [2]. The residual velocities, predicted by the proposed finite element simulation to vary with the impact velocities, are very close to the test results.

Some of the impact phenomena may not be considered well enough by the 2D finite element modeling. However, the residual velocities of the projectile predicted by the proposed methodology are well agreed with the test data. An advanced analysis will be conducted by 3D finite element codes in the future study.

4. Numerical analysis of oblique impact

This section presents an example of oblique impact. The projectile and the target are the same as those in the example of normal impact, but the projectile in this case impacts at an oblique angle. The angle θ between the projectile's trajectory and the outward normal of the target slab is defined as the angle of obliquity, which is depicted in Fig. 12. The proposed methodology predicts the trajectories of projectiles that penetrate the equivalent reinforced concrete slab at various angles of obliquity with an impact velocity of 743 m/s, from which the ricochet limit is also determined. The ricochet limit of an ogive-nose steel projectile at various impact velocities from 400 to 1100 m/s, is then investigated and compared with the results of Tate's formula [19]. The numerical techniques applied to the finite

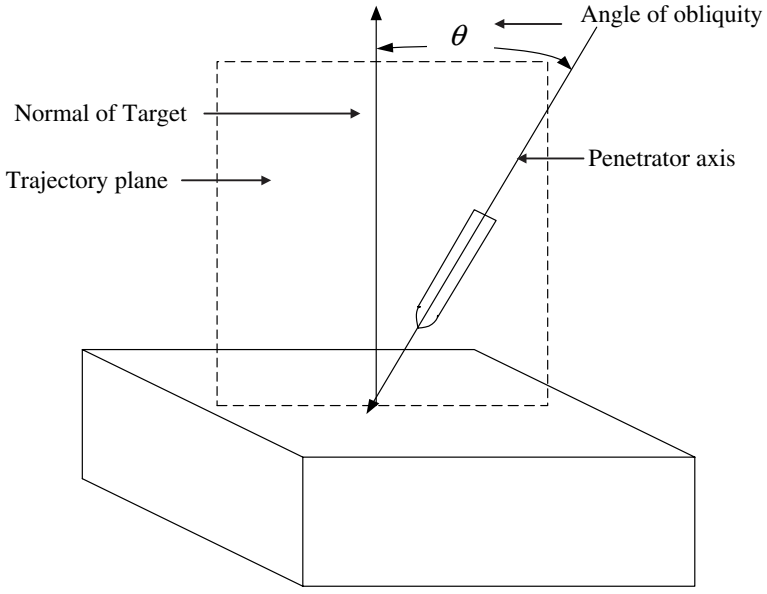

Fig. 12. Illustration of impact nomenclature.

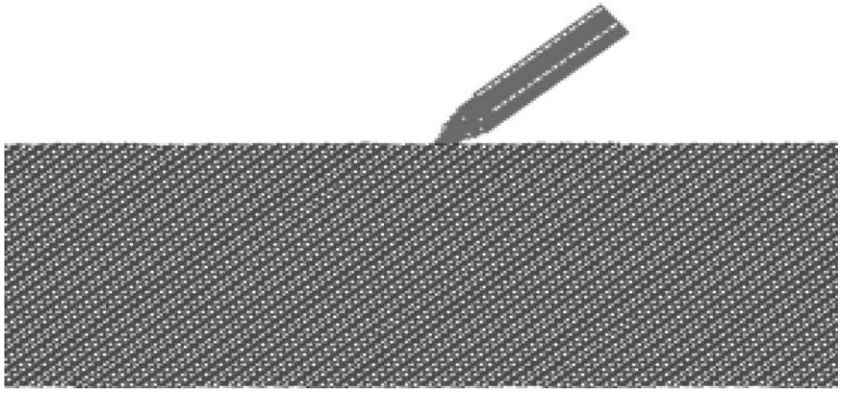

Fig. 13. Finite element model for θ angle oblique impact of reinforced concrete slab.

element analyses, including the erosion algorithm and the failure criterion, are the same as in the preceding section.

The term "ricochet" means that the projectile is deflected from the impact surface, without being stopped or passing through the target. Sometimes, the projectile may partially penetrate into the target surface along a curved trajectory and then emerge from the target surface with a reduced velocity. Here, the ricochet limit or the ricochet angle is defined as the angle at which the nose of the projectile will make no more than a shallow crater (to a depth of up to around one-half the diameter of the projectile) in the front surface of the target, before being deflected from the target's surface. The ricochet limit is the critical angle of obliquity for which the projectile will be deflected from the impact surface.

4.1. Projectile and target modeling

The oblique impact of an ogive-nose steel projectile at various impact velocities in a reinforced concrete slab with a thickness of 178 mm is considered. Fig. 13 depicts a finite element model of the oblique impact of an ogive-nose steel projectile with an angle of obliquity, θ. The model of the equivalent reinforced concrete target consists of 10,354 quadrilateral elements and 10,643 nodes under the plane strain assumption. The material properties and the erosion strains are the same as those in the case of normal impact.

4.2. Numerical results of oblique impact

The oblique impact of an ogive-nose projectile into an equivalent reinforced concrete slab at a velocity of

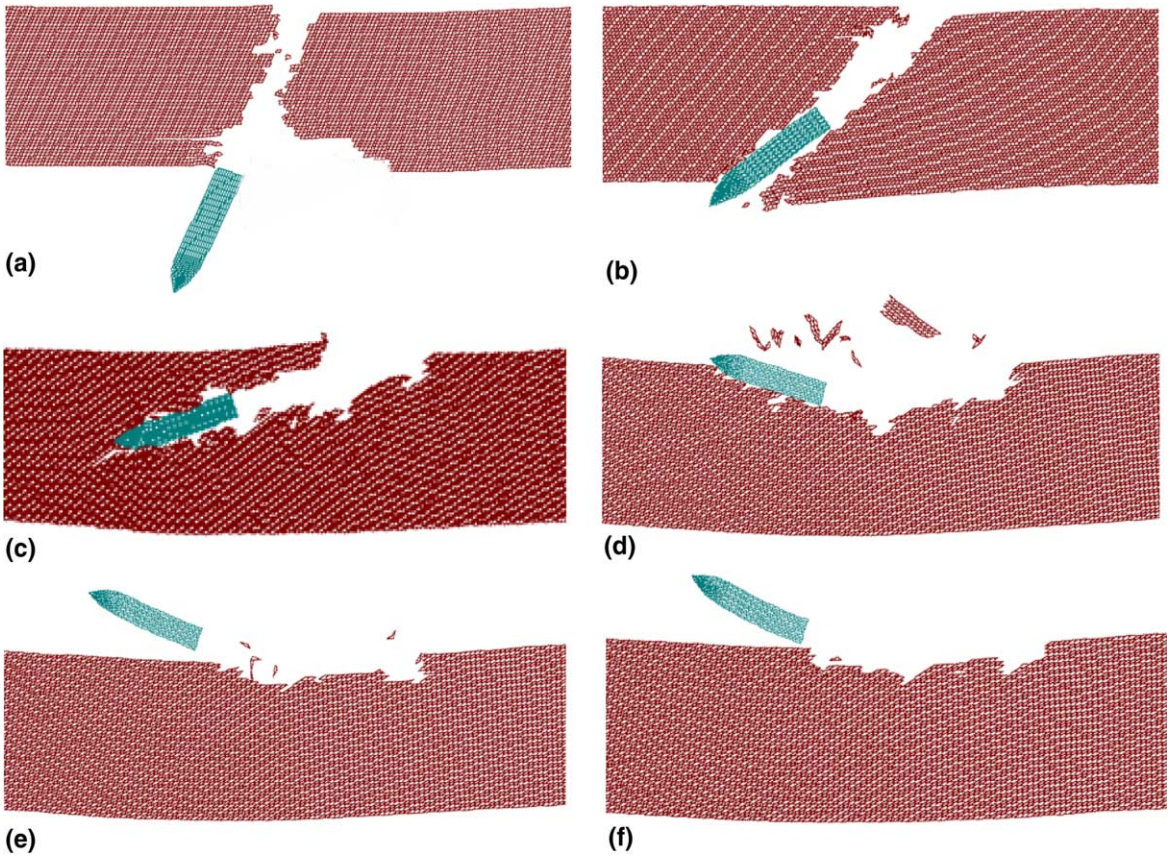

Fig. 14. (a) 20° obliquity impact for $V_s = 743$ m/s ($t = 580$ μs); (b) 40° obliquity impact for $V_s = 743$ m/s ($t = 480$ μs); (c) 50° obliquity impact for $V_s = 743$ m/s ($t = 640$ μs); (d) 58° obliquity impact for $V_s = 743$ m/s ($t = 720$ μs); (e) 60° obliquity impact for $V_s = 743$ m/s ($t = 720$ μs); (f) 61° obliquity impact for $V_s = 743$ m/s ($t = 720$ μs).

743 m/s is first investigated. Fig. 14(a)–(f) depict the trajectories of projectiles with various angles of obliquity. In Fig. 14(a), for a 20° oblique impact at 580 μs, the projectile creates a hole and successively perforates the target in the initial direction of the impact. Damage to the rear surface of the target also occurs. The formation of the path of penetration and the exit crater clearly generate intense shock waves after impact. The waves propagate into both the target and the projectile, causing the right side of the exit crater to bend outward (scabbing).

Fig. 14(b) plots the trajectory of the projectile for a 40° oblique impact at 480 μs. The steel projectile initially penetrates the target in the direction of impact and then follows a slightly upward trajectory until it finally perforates the target slab. The instantaneous radius of the tunnel depends on the nose shape of the projectile and the impact velocity.

At 55° obliquity, the projectile is embedded in the target slab at 640 μs after impact, as depicted in Fig. 14(c). Ricochet is expected to occur at a slightly greater obliquity. The angle of obliquity is slowly increased from 58° to 61° until the ricochet limit is reached.

Fig. 14(d)–(f) display the results for oblique impacts at 58°, 60° and 61°, respectively. In Fig. 14(d), showing the 58° oblique impact, the projectile makes a deeper crater (to a depth of about one-third the thickness of the slab) at the front surface of the target. In Fig. 14(e), for an impact obliquity of 60°, the crater is shallower than in the aforementioned case of 58° impacts. In Fig. 14(f), the impact obliquity is increased to 61°. The tangential velocity component (to the left) of the projectile exceeds the normal velocity component (downward); therefore, the projectile is deflected from the target with a clockwise rotation. The rotation of the projectile depends on the magnitudes of its normal and tangential velocity components, the combined rotational velocity and the frictional force applied by the target slab material. According to the numerical results presented above, the projectile ricochet limit is estimated to be 61° at an impact velocity of 743 m/s.

Ricochet limits for various impact velocities are of interest. Accordingly, a series of calculations were performed to predict the ricochet limits of an ogive-nose steel projectile against an equivalent reinforced concrete slab for a range of impact velocities from 400 to 1100 m/s. Fig. 15 shows numerically calculated ricochet limits for various impact velocities. The ricochet limit in-

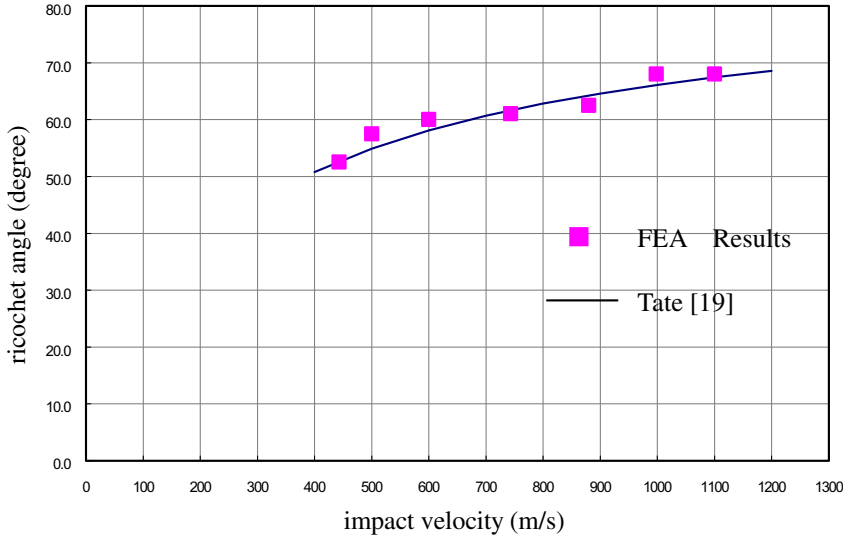

Fig. 15. Comparison of FEA numerical results and empirical formula of Tate [19].

crease with the impact velocity of the projectile, consistent with Tate's formula [19] as shown in Eq. (23)

$$\tan^3\beta = \frac{2}{3}\frac{\rho_p V^2}{Y_p}\left(\frac{l^2+d^2}{ld}\right)\left[1+\left(\frac{\rho_p}{\rho_t}\right)^{1/2}\right] \tag{23}$$

where β represents the ricochet angle; V is the impact velocity; l and d are the length and diameter of the projectile, respectively; ρ_p and ρ_t are the densities of the projectile and the target, respectively, and Y_p is a characteristic projectile strength which is closely related to the Hugoniot elastic limit of the material. A good agreement between the computational results and Tate's formula is obtained for a value of $Y_p = 7.5\times10^9$ GPa.

In Fig. 15, a calculation data point falls below the right side of the ricochet limit curve represents the perforation of the target by the projectile, penetration (the projectile makes a deep crater in the front surface of the target) or embedding in the target. Whereas, if the calculation yields a point on the ricochet limit curve or fall on the above left side of the curve, then the projectile will ricochet away from the impact surface.

The experimental results of similar oblique impact tests are not obtainable by the authors. Therefore, the numerically computational results are compared to the Tate's semi-empirical formula [19] for the ricochet limit as a function of the impact velocity qualitatively. However, the numerical methodology of modeling the oblique impact and the erosion criteria for the similar reinforced concrete target are identical to that of the previous example of the normal impact, which has been verified with the available test data. Thus, the numerical results should be controlled within a reasonable range of errors.

5. Conclusions

This paper applied the equivalent inclusion method to perform finite element analyses of reinforced concrete under oblique impact. The equivalent stiffness matrix of the reinforced concrete targets and the associated equivalent material moduli are derived for finite element analyses. The finite element meshes for the equivalent material of a reinforced concrete slab are as simple as those for a plain concrete material. No additional meshes are required for modeling of the reinforcing steel bars. The residual velocity and ricochet limit of an ogive-nose steel projectile, impacting equivalent reinforced concrete targets are examined using the proposed methodology.

A series of calculations are performed to predict the ricochet limit of an ogive-nose steel projectile that impacts a reinforced concrete slab at various velocities from 400 to 1100 m/sec. The numerically predicted ricochet limit is observed to increase with the impact velocity, which result is consistent with Tate's formula for the ricochet limit as a function of impact velocity. The numerical results are compared with Tate's formula. From the engineering perspective, finite element analyses based on the equivalent inclusion method is applicable and can feasibly predict the ricochet limit of a projectile against a reinforced concrete target.

The proposed model of the oblique impact of a projectile on reinforced concrete provides a practical tool for studying oblique impact on reinforced concrete slabs, especially for designers of military defense structures, weapon systems, nuclear power plants, and other facilities.

References

[1] Kasai Y, Tsubota H, Ohno T, Kogure K, Uchida T. Experimental study on impact resistance of reinforced concrete slabs with thin steel plates against projectile impact. Proc Int Symp Impact Eng 1992:211–6.

[2] Hanchak SJ, Forrestal MJ, Young ER, Ehrgott JQ. Perforation of concrete slabs with 48 MPa (7 ksi) and140 MPa (20 ksi) unconfind compressive strengths. Int J Impact Eng 1992;12(1):1–7.

[3] Dancygier AN, Yankelevsky DZ. High strength concrete response to hard projectile impact. Int J Impact Eng 1996;18(6):583–99.

[4] Dancygier AN, Yankelevsky DZ. Penetration mechanisms of non-deforming projectiles into reinforced concrete barriers. Struct Eng Mech 2002;13(2):171–86.

[5] Gomez JT, Shuka A. Multiple impact penetration of semi-infinite concrete. Int J Impact Eng 2001;25:965–79.

[6] Kar AK. Projectile penetration into buried structures. J Struct Div, Proc Amer Soc Civil Engrs 1978;104(ST1):125–39.

[7] Haldar A, Hamieh HA. Local effect of solid missiles on concrete structures. J Struct Eng 1984;110(5):948–60.

[8] Adeli H, Amin AM. Local effect of impactors on concrete structures. Nucl Eng Des 1985;88:301–17.

[9] McMahon P, Meyers BL, Buchert KP. Impact of deformable missiles on concrete walls. J Power Div, Proc Amer Soc Civil Engrs 1978;104(PO1):183–97.

[10] Chang WS. Impact of solid missiles on concrete barriers. J Struct Div, Proc Amer Soc Civil Engrs 1981;107(ST2):257–71.

[11] Williams MS. Modeling of local impact effects on plain and reinforced concrete. ACI Struct J 1994;91(2):179–87.

[12] Yankelevsky DZ. Local response of concrete slabs to low velocity missile impact. Int J Impact Eng 1997;19(4):331–43.

[13] Forrestal M, Tzou DY. A spherical cavity-expansion model for concrete targets. Int J Solids Struct 1997;34(31–32):4127–46.

[14] Sawamoto Y, Tsubota H, Kasai Y, Koshika N, Morikawa H. Analytical studies on local damage to reinforced concrete structures under impact loading by discrete element method. Nucl Eng Des 1998;179:157–77.

[15] Chu YA, Wang JP. A numerical study on penetration and underground detonation damage of concrete target. The 13th International Symposium on Ballistics Stockholm, Sweden,1992. p. 1–3.

[16] Chen EP. Numerical implementation of a brittle damage model and its application to concrete slab perforation. PVP-Vol.343, Development, Validation, and Application of Inelastic Methods for Structural Analysis and Design ASME 1996; 147–52.

[17] Ågårdh L, Laine L. 3D FE-Simulation of high velocity fragment perforation of reinforced concrete slabs. Int J Impact Eng 1999; 22(4):911–22.

[18] Schewr LE, Day J. Computational techniques for penetration of concrete and steel targets by oblique impact of deformable projectiles. Nucl Eng Des 1991;125:215–38.

[19] Tate A. A simple estimate of the minimum target obliquity required for the ricochet of a high speed long rod projectile. J Phys D: Appl Phys 1979;12:1825–9.

[20] Eshelby JD. The determination of the elastic field of an ellipsoidal inclusion, and related problems. Proc Royal Soc Lond 1957;A241: 376–96.

[21] Eshelby JD. The elastic field outside an ellipsoidal inclusion. Proc Royal Soc Lond 1959;A252:561–9.

[22] Mori T, Tanaka K. Average stress in matrix and average elastic energy of materials with misfitting inclusion. Acta Metall 1973;21: 571–4.

[23] Yang CC, Huang R. A two-phase model for predicting the compressive strength of concrete. Cement Concr Res 1996;26(10): 1567–77.

[24] Mura T. Micromechanics of defects in solids. 2nd revised ed. Netherlands: Kluwer Academic Publishers; 1987.

[25] Chao LP, Hung JH. Prediction of elastic moduli of porous materials with equivalent inclusion method. J Reinforced Plast Compos 1999;18(7):592–605.

[26] Hung JH. Effective electroelastic moduli of multiphase piezoelectric composites. J Chinese Soc Mech Engrs, Taiwan 1996;17(2): 111–21.